Influence of copper telluride nanodomains on the transport properties of n-type bismuth telluride

Yu Zhang,[a†] Congcong Xing,[a†] Yu Liu,[a,b*] Mengyao Li,[a] Ke Xiao,[a] Seungho Lee, [b] Xu Han,[c] Ahmad Ostovari Moghaddam,[d] Jordi Arbiol,[c,e] Maria Ibáñez,[b] Kai Pan,[f] Ying Xie,[f*] Andreu Cabot[a,e*]

[a] Catalonia Energy Research Institute - IREC, Sant Adrià de Besòs, 08930 Barcelona, Spain.

[b] IST Austria, Am Campus 1, 3400 Klosterneuburg, Austria.

[c] Catalan Institute of Nanoscience and Nanotechnology (ICN2), CSIC and BIST, Campus UAB, Bellaterra, 08193 Barcelona, Catalonia, Spain.

[d] South Ural State University, 76, Lenin Ave., Chelyabinsk 454080, Russia

[e] ICREA, Pg. Lluis Companys 23, 08010 Barcelona, Catalonia, Spain.

[f] Key Laboratory of Functional Inorganic Material Chemistry, Ministry of Education, Heilongjiang University, 150080, Harbin, PR China

[†] These authors contributed equally to this work.

*Corresponding author E-mail: yu.liu@ist.ac.at; xieying@hlju.edu.cn; acabot@irec.cat.

Abstract: The high processing cost, poor mechanical properties and moderate performance of Bi_2Te_3–based alloys used in thermoelectric devices limit the cost-effectiveness of this energy conversion technology. Towards solving these current challenges, in the present work, we detail a low temperature solution-based approach to produce Bi_2Te_3-$Cu_{2-x}Te$ nanocomposites with improved thermoelectric performance. Our approach consists in combining proper ratios of colloidal nanoparticles and to consolidate the resulting mixture into nanocomposites using a hot press. The transport properties of the nanocomposites are characterized and compared with those of pure Bi_2Te_3 nanomaterials obtained following the same procedure. In contrast with most previous works, the presence of $Cu_{2-x}Te$ nanodomains does not result in a significant reduction of the lattice thermal conductivity of the reference Bi_2Te_3 nanomaterial, which is already very low. However, the introduction of $Cu_{2-x}Te$ yields a nearly threefold increase of the power factor associated to a simultaneous increase of the Seebeck coefficient and electrical conductivity at temperatures above 400 K. Taking into account the band alignment of the two materials, we rationalize this increase by considering that $Cu_{2-x}Te$ nanostructures, with a relatively low electron affinity, are able to inject electrons into Bi_2Te_3, enhancing in this way its electrical conductivity. The simultaneous increase of the Seebeck coefficient is related to the energy filtering of charge carriers at energy barriers within Bi_2Te_3 domains associated with the accumulation of electrons in regions nearby a $Cu_{2-x}Te/Bi_2Te_3$ heterojunction. Overall, with the incorporation of a proper amount of $Cu_{2-x}Te$ nanoparticles, we demonstrate a 250% improvement of the thermoelectric figure of merit of Bi_2Te_3.

Keywords: Bi_2Te_3, nanocomposites, energy filtering effect, $Cu_{2-x}Te$, thermoelectricity.

1. Introduction

Thermoelectric (TE) devices, able to convert temperature gradients into electricity and *vice versa*, have a plethora of potential applications, especially around ambient temperature. However, their use is frequently limited by insufficient cost-effectiveness, related both to a moderate efficiency and a relatively high cost. The efficiency of TE devices is determined by three interdependent material parameters: electrical conductivity (σ), Seebeck coefficient (S), and thermal conductivity (κ), which are combined in a dimensionless figure of merit $ZT=\sigma S^2 T\kappa^{-1}$[1-4]. On the other hand, the elevated cost of current TE devices, optimized toward cooling applications, is related to the large amount of highly crystalline Bi-Sb-Te-Se alloys used to manufacture them. To cut costs, devices aimed at harvesting small temperature gradients could strongly reduce the amount of TE material used. Besides, the use of high crystallinity materials is not only unnecessary but even detrimental to the device performance as crystalline materials have associated higher thermal conductivities and poorer mechanical properties than their polycrystalline counterparts.

Bottom-up strategies based on solution-processed building blocks offer additional advantages in both directions. Properly designed and engineered nanocomposites allow to partially decouple TE properties, adjusting the charge carrier concentration without significantly reducing the mobility by modulation doping, increasing the Seebeck coefficient through energy filtering and quantum confinement, and reducing thermal conductivity through extensive phonon scattering[5-19]. At the same time, because bottom-up approaches do not require the large scale organization of atoms into macroscopic crystal domains, the energy usage, processing time and thus the overall production cost can be strongly reduced. As a bonus advantage, beyond providing improved TE properties at a potentially lower cost, nanomaterials allow improving mechanical performances, especially for layered materials such as Bi_2Te_3, which are particularly fragile toward fracture along van der Waals planes.

In the last decade, several strategies have been developed to further improve the TE properties of Bi_2Te_3-based alloys[20-30]. One successful approach to increasing the power factor (σS^2) and at the same time reduce the thermal conductivity has been the incorporation of doping elements, such as Cu. Besides promoting phonon scattering, the incorporation of Cu allows optimizing the charge carrier concentration by introducing additional carriers. These extra carriers have been shown to significantly increase electrical conductivity while moderately decreasing Seebeck coefficients, overall translating into higher power factors and figures of merit.[31-39] Cu ions electronically dope Bi_2Te_3 in different ways, depending on the conductivity type of the Bi_2Te_3-based alloy and the Cu concentration and location. When Cu^+ ions intercalate at the van der Waals gap between Bi_2Te_3 layers, they act as donors.[36, 39] In contrast, Cu^+ ions substituting Bi act as acceptors[36, 38]. Moreover, the presence of Cu may modify the concentration of electroactive defects within Bi_2Te_3-based alloys, altering the amount of Te vacancies and Bi and Te antisites, for instance.[37] Besides, amounts of Cu above the solubility limit lead to the segregation of $Cu_{2-x}Te$ phases. This segregation reduces the amount of Te within the alloy and consequently increases the amount of Te vacancies and/or reduces the concentration of Te antisites, both acting as electron donors[36-38]. Additionally, the presence of $Cu_{2-x}Te$ domains within the Bi_2Te_3 matrix can electronically affect the material in ways that remain largely unexplored. $Cu_{2-x}Te$ is generally characterized by a relatively low work function[40] and a degenerated p-type conductivity associated with its Cu deficiency.[10, 41-44] Thus, in $Bi_2Te_3/Cu_{2-x}Te$ heterostructures, $Cu_{2-x}Te$ is most probably able to inject charge carriers into Bi_2Te_3[45].

In this work, we produce Bi_2Te_3-$Cu_{2-x}Te$ nanocomposites with controlled phase ratio by mixing proper amounts of Bi_2Te_3 and $Cu_{2-x}Te$ colloidal nanoparticles. We characterize their structural and chemical properties and discuss their TE performance taking into account the heterojunctions formed between the two materials.

2. Materials and methods

2.1 Chemicals and solvents

Oleylamine (OAm, technical grade 70%), oleic acid (OAc, technical grade 90%), bismuth(III) chloride ($BiCl_3$, ≥ 98%), copper(II) acetate monohydrate ($Cu(AC)_2$, $(CH_3COO)_2Cu{\cdot}H_2O$, ≥ 98%), tellurium dioxide (TeO_2, ≥99%), potassium hydroxide (KOH, ≥ 98%), hydrazine monohydrate ($NH_2NH_2{\cdot}H_2O$, 64~65%) and polyvinylpyrrolidone (PVP, $(C_6H_9NO)_n$, average molecular weight ~55,000) were purchased from Sigma Aldrich. Tri-n-octylphosphine (TOP, 97%) was purchased from Strem. Ethylene glycol (EG, $HOCH_2CH_2OH$, 99%) was purchased from Fisher. Analytical grade ethanol, isopropanol and acetone were obtained from various sources. All chemicals were used as received without further purification. Syntheses were carried out using a standard vacuum/dry argon Schlenk line.

2.2 Synthesis of bismuth telluride nanowires

Bi_2Te_3 nanowires were synthesized following a previously reported protocol.[46] In a typical synthesis, a mixture of 5.6 mmol of TeO_2, 56 mL of EG, 37 mmol of KOH, and 1.5 g of PVP were added into a three-neck flask and heated to 140 °C to completely dissolve them. Afterwards, 0.87 mL hydrazine monohydrate was injected to reduce Te and the solution was maintained at 140 °C for 1 h. These initial steps resulted in the formation of Te nanowires as described previously.[13, 45, 46] Then the temperature was raised to 160 °C and a hot solution of $BiCl_3$/EG was injected into the flask. The hot $BiCl_3$/EG solution was prepared by adding 3.6 mmol $BiCl_3$ into 15 mL EG in a glass vial that was heated to 100−120 °C before injection. The $BiCl_3$ solution was allowed to react with the tellurium nanowires for 1 h at 160 °C. After that, the mixture was cooled down naturally to room temperature. The products were firstly purified by adding acetone and centrifuging. Then ethanol was used to redisperse the particles and acetone was used as antisolvent to precipitate them. In the next step, deionized water was introduced to dissolve remaining impurities and products were precipitated by slow

centrifugation. This procedure was repeated twice. In the last step, particles were dispersed in ethanol and precipitated with acetone. The final products were dried under vacuum and stored in an Ar-filled glovebox until posterior use.

2.3 Synthesis of copper telluride nanoparticles

A tellurium precursor solution (TOPTe) was prepared in an argon-filled glovebox one week before synthesis: 6.38 g tellurium powder (0.05 mol) was dissolved in 100 mL TOP to form the 0.5 M TOPTe which had a clear yellow color. In a typical synthesis of $Cu_{2-x}Te$ colloidal nanoparticles, 0.3 mmol of $Cu(AC)_2$ was mixed with 6 ml of OAm in a 25 mL three-neck flask. The mixture was kept under vacuum for 20 min at room temperature, then heated to 120 ºC and maintained at this temperature for 60 min still under vacuum to obtain a clear solution and remove low boiling point impurities. Then the temperature was increased to 220 ºC under Ar. After ~10 min, the initial bright yellow solution became clear light brown. At this point, 1.5 mL of 0.5 M TOPTe was injected and the light brown solution immediately changed color to deep green. Upon injection, the temperature of the reaction mixture dropped to ~210 ºC. The mixture was allowed to recover the 220 ºC and maintained at this point for 1 h. Afterwards, the colloidal solution was rapidly cooled to room temperature with a water bath at an initial approximate rate of ~80 ºC/min. During the cooling down process, when the solution reached ~70 ºC, 2 mL of OAc were added to replace the weakly bound OAm molecules. Finally, 5 mL of chloroform were added to the crude solution and the mixture was sonicated for several minutes. The final deep green product was precipitated by centrifugation at 8000 rpm for 5 min. Then it was redispersed in chloroform and precipitated one more time by centrifugation in the presence of isopropanol. Finally, $Cu_{2-x}Te$ nanoparticles were re-dispersed in chloroform and kept in an Ar-filled glovebox until their posterior use.

2.4 Nanomaterial consolidation

Bi_2Te_3 and $Cu_{2-x}Te$ nanoparticles were mixed at the proper ratio in hexane solution. The mixture

was sonicated for 1 h to obtain a homogeneous dispersion. Then the nanoparticles were dried out from the solvent. The obtained nanopowder was introduced inside a tube furnace and annealed at 450 °C for 1 h under an Ar flow. The annealed material was loaded into a graphite die and uniaxially hot-pressed into cylinders (Ø 10 mm×10 mm) using a custom-made hot-press. This process was carried out within an argon-filled glove box. The hot press temperature was set at 290 ºC and the pressure was increased up to 50 MPa for 5 min. Relative densities of the consolidated pellets were measured by the Archimedes' method. From these cylinders, rectangular bars of about 6 × 6 × 1 mm^3 were cut in two normal directions, along and normal to the pressure axis.

2.5 Structural and chemical characterization

The morphology and size of the nanoparticles were characterized by transmission electron microscopy (TEM) using a Zeiss Libra 120, operating at 120 kV, and field-emission scanning electron microscopy (SEM) on an Auriga Zeiss operated at 5.0 kV. X-ray diffraction (XRD, 2θ angle: 20° to 60°; scanning rate: 2°/min) analyses were carried out on a Bruker AXS D8 Advance X-ray diffractometer with Cu–Kα radiation (λ = 1.5406 Å). Chemical composition and crystallographic structure were analyzed by high-resolution TEM (HRTEM) and electron energy loss spectroscopy (EELS) using a Tecnai F20 field-emission gun microscope at 200 keV embedded with a Gatan Quantum image filter. Additionally, the nanoparticles composition was analyzed using an Oxford energy dispersive X-ray spectrometer (EDX) combined with a Zeiss Auriga SEM at 20.0 kV.

2.6 Thermoelectric property measurement

Electrical resistivity data was obtained using a standard four-probe method. Seebeck coefficients were determined using a static DC method. Electrical resistivity and Seebeck coefficients were measured simultaneously in a LSR-3 Linseis system under a helium atmosphere, in the temperature range between room temperature and 573 K. 3 measurements

were taken at each temperature in each temperature cycle. Considering the system accuracy and the measurement precision, an error of *ca.* 5 % in the measurement of the electrical conductivity and Seebeck coefficients was estimated. The thermal conductivity was calculated according to $\kappa = \lambda C_p \rho$, where κ is the total thermal conductivity, λ is the thermal diffusivity, C_p is heat capacity, and ρ is the measured density of each specimen. An XFA 600 xenon flash apparatus was applied to measure the thermal diffusivities (λ) of the samples with an estimated error of ca. 5 %. *Cp* was calculated from empirical formulas by the Dulong–Petit limit (3R law), and the density (ρ) values used here were measured using the Archimedes' method. Hall charge carrier concentrations (n_H) and mobilities (μ_H) at room temperature (300 K) and high temperature (300-600 K) were obtained from the Van der Pauw method using a magnetic field of 1 T (ezHEMS, NanoMagnetics). Values provided correspond to the average of 7 measurements, from which an error of ca. 10% was estimated.

3. Result and discussion

Bi_2Te_3 was prepared using a previously reported two-step process based on the reaction of Bi with Te nanowires (see details in the experimental section)[46]. The obtained particles displayed a uniform nanowire geometry with a narrow distribution of diameters (30±10 nm) and lengths (600 ± 80 nm) as observed by TEM (Figure 1a, b). XRD analysis showed the Bi_2Te_3 nanowires to be highly crystalline with the Bi_2Te_3 rhombohedral phase (JCPDS NO. 01-082-0358, Figure 1d). HRTEM characterization confirmed the Bi_2Te_3 rhombohedral phase (space group = R-3M) with a=b= 4.2999 Å and c= 30.5975 Å. EELS elemental composition maps revealed the homogeneous composition of the nanowires (Figure 1c).

$Cu_{2-x}Te$ nanocrystals were prepared by reacting a solution of $Cu(Ac)_2$ with TOPTe at 220 ºC in OAm (see materials and methods section). Figure 1e shows a representative TEM micrograph of the as-synthesized $Cu_{2-x}Te$ nanoparticles that displayed a cubic/rectangular morphology with a relatively narrow size distribution. HRTEM characterization allowed

assigning the crystal structure of the nanoparticles to a $Cu_{1.5}Te$ cubic phase (space group = Pm-3n) with a=b=c=7.5100 Å (Figure 1f), consistently with previous reports.[47, 48]. The reference XRD pattern simulated from the cubic $Cu_{1.5}Te$ crystal phase determined by HRTEM fitted well the experimental results obtained from the XRD characterization of the material (Figure 1d). EELS elemental composition maps showed a homogeneous distribution of the two elements within the $Cu_{2-x}Te$ nanoparticles (Figure 1g).

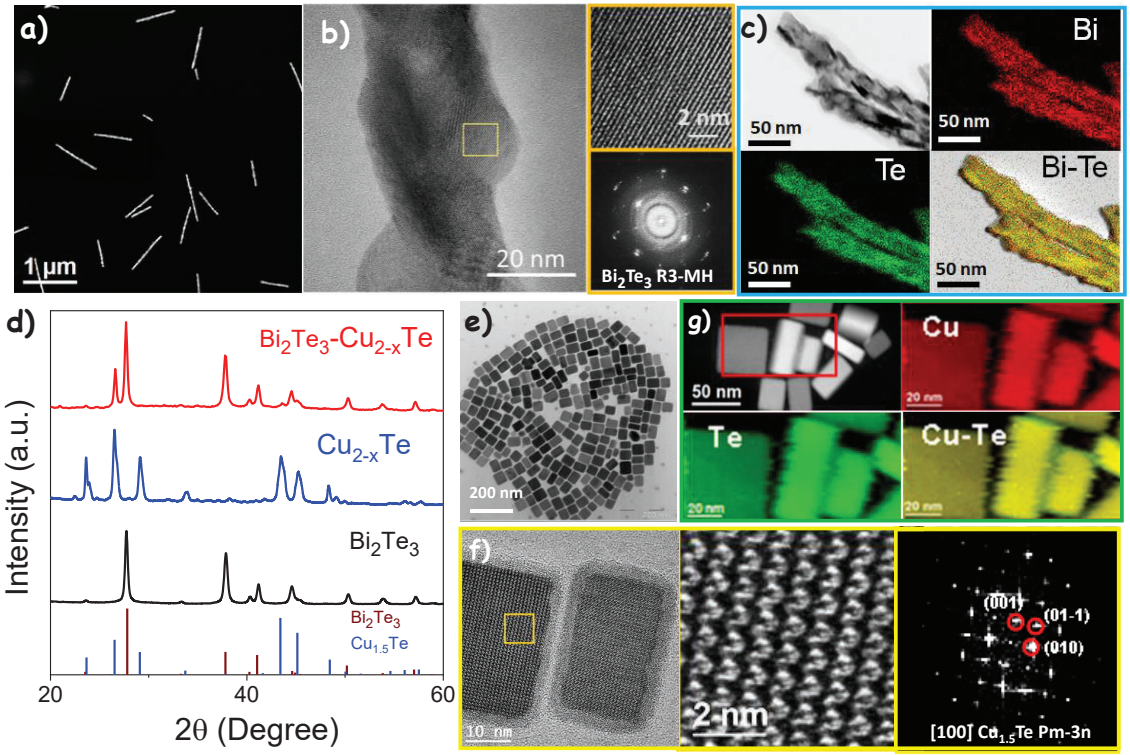

Figure 1. (a) Representative high-angle annular dark-field scanning transmission electron microscopy (HAADF-STEM) and bright-field TEM micrographs of Bi_2Te_3 nanowires. (b) HRTEM micrograph, detail of the orange squared region and its corresponding power spectrum. (c) STEM micrograph and EELS chemical composition maps obtained from the red squared area in the STEM micrograph. Bi $N_{6,7}$-edge at 157 eV (red), Te $M_{4,5}$-edge at 572 eV (green). (d) Powder XRD pattern of as-synthesized Bi_2Te_3 and $Cu_{2-x}Te$ nanoparticles and of a consolidated Bi_2Te_3-$Cu_{2-x}Te$ nanocomposite. The reference pattern for Bi_2Te_3 (JCPDS 01-082-0358) and the simulated XRD pattern of $Cu_{1.5}Te$ are also displayed. (e) Representative TEM image of $Cu_{2-x}Te$ nanocubes. (f) HRTEM micrograph, detail of the yellow squared region and its corresponding power spectrum. The $Cu_{1.5}Te$ lattice fringe distances were measured to be

0.708 nm, 0.528 nm and 0.731 nm, at 45.68º and 86.43º, which was interpreted as the $Cu_{1.5}Te$ cubic phase, visualized along its [100] zone axis. (g) STEM micrograph and EELS chemical composition maps obtained from the red squared area in the STEM micrograph. Cu $L_{2,3}$-edges at 931 eV (red), Te $M_{4,5}$-edge at 572 eV (green).

Colloidal Bi_2Te_3 nanowires and $Cu_{2-x}Te$ nanocrystals were mixed at proper mass ratios ($0 \leq Bi:Cu \leq 26$) in hexane (Figure 2a). SEM characterization of the dried mixture revealed a homogeneous dispersion of the two types of particles (Figure 2b). After solvent evaporation, the obtained Bi_2Te_3-$Cu_{2-x}Te$ nanopowder was annealed at 450 °C to remove organic residues. After this process, particles maintained their initial geometry and crystal phase, and both phases remained homogeneously dispersed (Figures S1, 2c).

Afterwards, the annealed powder was loaded inside a graphite die and hot-pressed into cylindrical pellets that achieved relative densities in the range 85-89 % (Table S1). XRD patterns of the Bi_2Te_3-$Cu_{2-x}Te$ pellets showed the main peaks of the Bi_2Te_3 phase and a smaller XRD peak at $2\theta = 26.7º$ that was assigned to the $Cu_{1.5}Te$ phase (Figure 3a). SEM characterization showed the consolidated pellet to be formed of elongated structures resembling the initial Bi_2Te_3 nanowires, with no obvious grain growth after hot pressing (Figure 2d). EDX analysis of the Bi:Cu=21 composite showed a Cu/Bi/Te molar ratio around 1/7.6/11.4, i.e. a Te/(Bi+Cu) molar ratio close to the stoichiometric 3/2. Similar Te/(Bi+Cu) ratios were obtained for Bi:Cu=13 and Bi:Cu=26 samples (Figure S2). Additionally, EDX compositional maps showed a relatively homogeneous distribution of Cu at a 5 μm scale (Figure 3b).

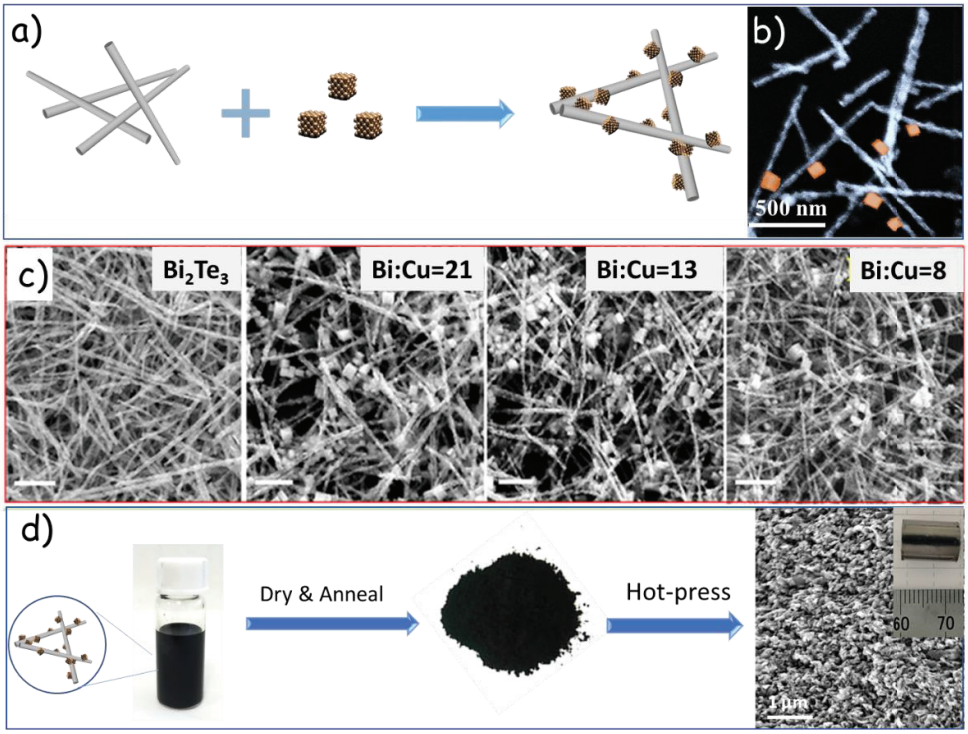

Figure 2. (a) Schematic illustration of the preparation of Bi_2Te_3-$Cu_{2-x}Te$ nanocomposites. (b) SEM image of the dried mixture of $Cu_{2-x}Te$ and Bi_2Te_3 nanoparticles. (c) SEM images of annealed Bi_2Te_3 and Bi_2Te_3-$Cu_{2-x}Te$ nanopowders. Scale bars = 200 nm. (d) Schematic illustration of sample processing, including optical photographs of the initial colloidal dispersion of the two types of particles, the dried powder and the final pellet, and a cross-section SEM image of the hot-pressed material.

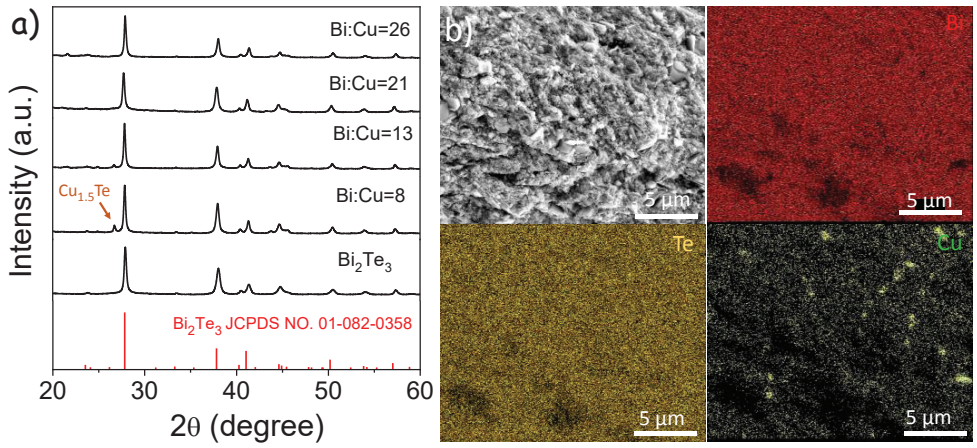

Figure 3. (a) XRD pattern of consolidated Bi_2Te_3-$Cu_{2-x}Te$ pellets with different compositions. (b) SEM micrograph of a Bi_2Te_3-$Cu_{2-x}Te$ (Bi:Cu=21) pellet and corresponding EDX composition maps for Bi (red), Te (orange) and Cu (green).

The TE properties of Bi_2Te_3-$Cu_{2-x}Te$ nanocomposites were characterized along two directions: parallel and normal to the pressure axis (Figure S3). Despite the asymmetric geometry of the Bi_2Te_3 building blocks used to produce the composites and the anisotropic crystal structure of Bi_2Te_3, similar transport properties were obtained in both directions. We associate this experimental result to the random orientation of the crystallites within the nanocomposite, i.e. to the lack of crystallographic texture. SEM characterization confirmed the long-range random distribution of crystal domains (Figure 4c, d). Additional XRD characterization of the samples being hold in the two normal directions displayed similar relative peak intensities ($I_{(0015)}/I_{(110)}$), further confirming the homogeneous orientation of the Bi_2Te_3 crystal domains (Figure 4a,b). On the grounds of lacking anisotropic transport properties, in the following, we focus on discussing the results obtained from the direction normal to the pressure axis.

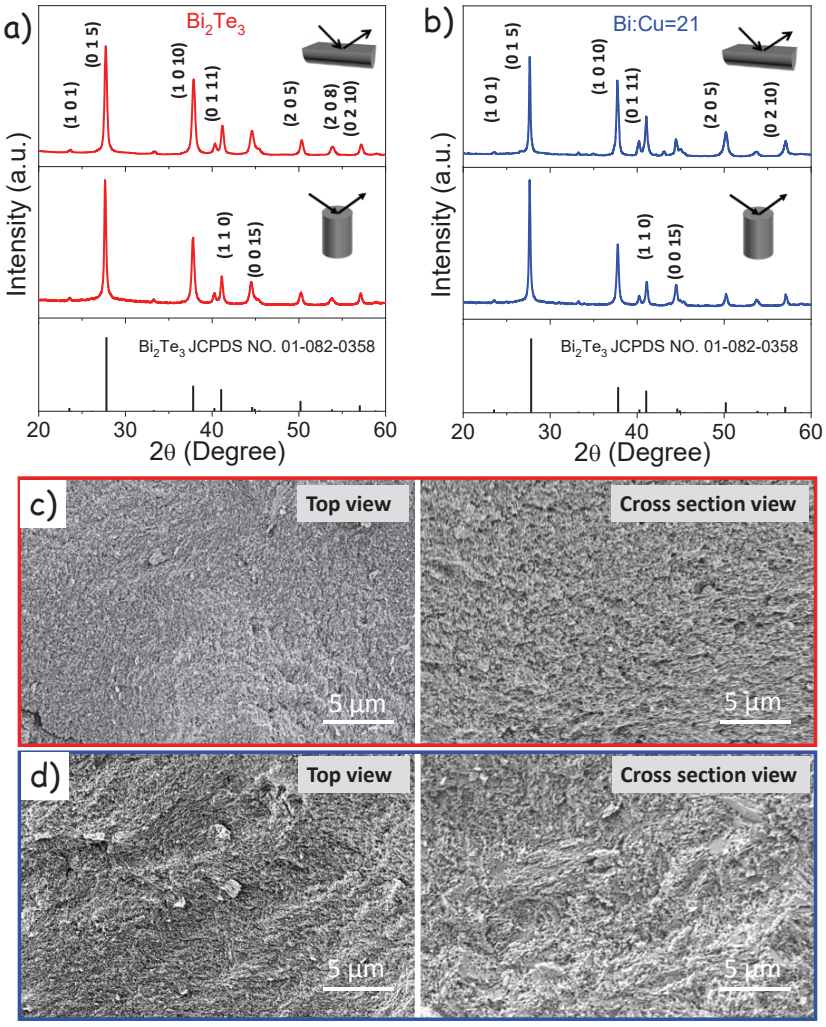

Figure 4. (a,b) XRD patterns of consolidated (a) Bi_2Te_3 and (b) Bi_2Te_3-$Cu_{1.5}Te$ (Bi:Cu=21) pellets in two normal directions, perpendicular and parallel to the pressure axis, as marked within the graphs. (c,d) Top-view and cross-section SEM micrographs of consolidated (c) Bi_2Te_3 and (b) Bi_2Te_3-$Cu_{1.5}Te$ (Bi:Cu=21) pellets.

Figure 5 shows the TE properties of a series of Bi_2Te_3-$Cu_{2-x}Te$ nanocomposites obtained by combining different amounts of Bi_2Te_3 and $Cu_{2-x}Te$ particles (Bi:Cu=13, 21 and 26). The data obtained from a nanocrystalline Bi_2Te_3 sample produced by annealing and hot pressing Bi_2Te_3 nanowires is also plotted as a reference. The data obtained from a $Cu_{2-x}Te$ pellet produced by hot-pressing $Cu_{2-x}Te$ nanoparticles is provided in Figure S4.

AT room temperature, Bi_2Te_3 displayed moderate electrical conductivities (~ 10^4 S m^{-1}) and Seebeck coefficients (~ 130 μV K^{-1}), which slowly increased with temperature (Figure 5a,b). The incorporation of $Cu_{2-x}Te$ resulted in a slight decrease of the room temperature electrical conductivity and Seebeck coefficient (Figure 5a,b), which translated into lower power factors (Figure 5c). On the other hand, the $Cu_{2-x}Te$ pellet showed much larger electrical conductivities (0.8 x 10^6 S m^{-1}) but much lower Seebeck coefficients (0.5 μV K^{-1}, Figure S4).

Hall measurements showed the room temperature charge carrier concentration to increase with the presence of $Cu_{2-x}Te$, from n = 1.4x10^{19} cm^{-3} for Bi_2Te_3 to n = 1.8 x 10^{19} cm^{-3} for Bi_2Te_3-$Cu_{1.5}Te$ (Bi:Cu=18, Figure 6). On the other hand, the Hall charge carrier concentration of the $Cu_{2-x}Te$ pellet was much higher, p = 3.7 x 10^{21} cm^{-3}. We associate the larger charge carrier concentration obtained in Bi_2Te_3-$Cu_{1.5}Te$ composites with the spillover of charge carriers from the $Cu_{2-x}Te$ phase to the Bi_2Te_3 matrix, in line with the much lower electronic affinity of the former and its highly degenerated semiconductor character[22, 26]. On the other hand, carrier mobilities decreased with the presence of $Cu_{2-x}Te$ (Figure 6b), consistently with a promoted charge carrier scattering.

Taking into account the Hall charge carrier concentration and mobilities, the lower electrical conductivity measured at ambient temperature in Bi_2Te_3-$Cu_{2-x}Te$ nanocomposites compared with bare Bi_2Te_3 was associated with the lower electron mobilities within the composites. On the other hand, the lower Seebeck coefficients measured at ambient temperature were consistent with the larger charge carrier concentrations measured in the nanocomposites, as observed with a Pisarenko plot using a single parabolic band model and an effective mass $m^*=0.40\ m_0$ (Figure 6d).

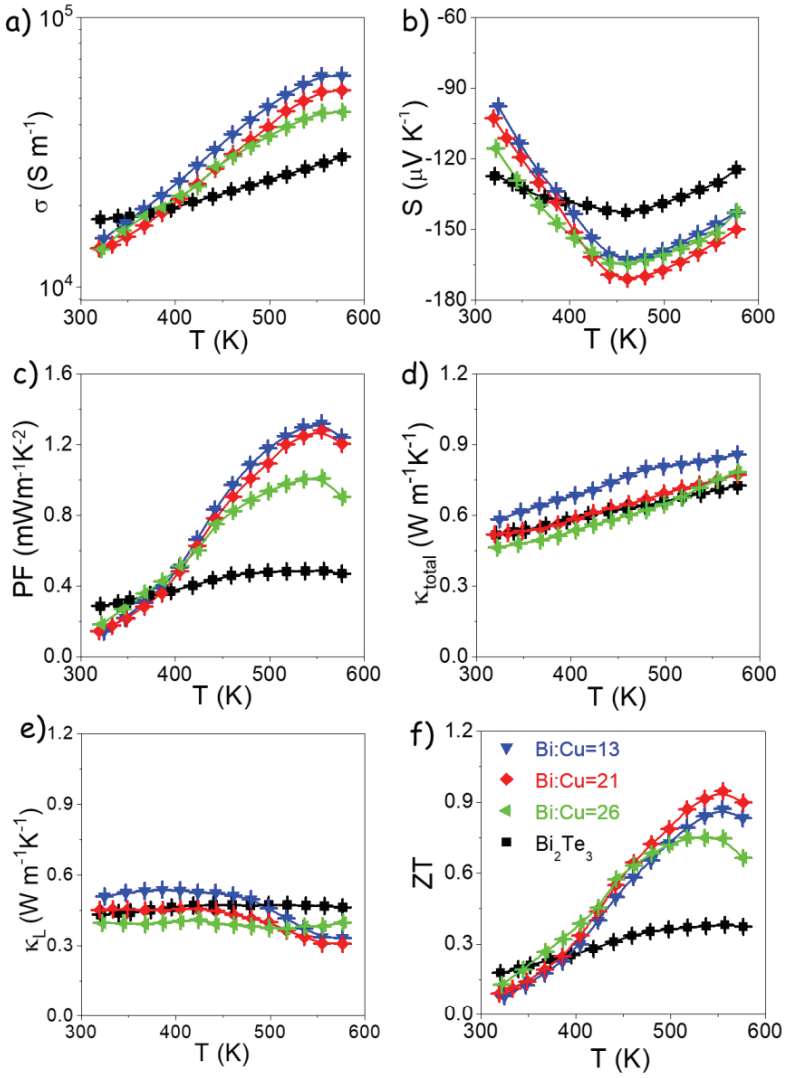

Figure 5. Temperature dependence of TE properties of Bi_2Te_3-$Cu_{2-x}Te$ pellets: (a) electrical conductivity, σ; (b) Seebeck coefficient, S; (c) power factor or $S^2\sigma$; (d) total thermal conductivity, κ_{total}; (e) lattice thermal conductivity, κ_L; (f) TE figure of merit, ZT.

All nanocomposites were characterized by strong dependences of the electrical conductivity and Seebeck coefficient with temperature. This strong temperature dependence was ascribed to the important role played by energy barriers on the charge transport properties, i.e. charge carriers strongly relied on an activation energy to move through nanocomposites. This activation energy was estimated at 130 meV from a linear fit of $Ln(\sigma T^{1/2})$ with $(kT)^{-1}$. As the temperature increased, the electrical conductivity of nanocomposites increased up to values

two to threefold higher than those of bare Bi_2Te_3. The absolute value of the Seebeck coefficient showed a parallel evolution, strongly increasing up to 460 K, but decreasing at higher temperatures when bipolar effects became dominant. Surprisingly, despite the larger charge carrier concentrations measured in nanocomposites and associated to the electron spillover from $Cu_{2-x}Te$ to Bi_2Te_3, nanocomposites were also characterized by much higher Seebeck coefficients at temperatures above 400 K (Figures 5b). These abnormally high Seebeck coefficients are more clearly perceived when plotting data within a Pisarenko plot, as displayed in Figure 6d. Overall, in all Bi_2Te_3-$Cu_{2-x}Te$ composites, the concomitant increase of electrical conductivity and Seebeck coefficient resulted in a significant increase of the power factor, up to 1.32 at 554 K.

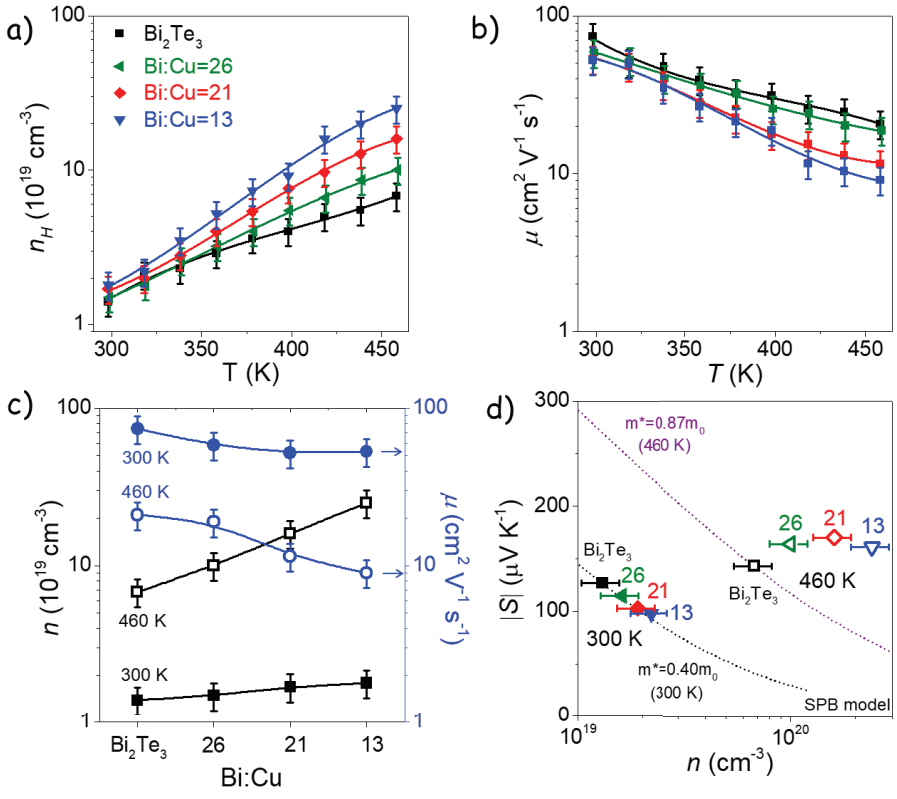

Figure 6. (a) Temperature dependence of the Hall charger carrier concentration and (b) mobility for Bi_2Te_3 and Bi_2Te_3-$Cu_{2-x}Te$ (Bi:Cu = 13, 21, 26). (c) Dependence of the charge carrier concentration and mobility on the Bi:Cu ratio at two temperatures, 300 K and 460 K. d) |S| vs. n for the different samples at 300 K (solid symbols) and 460 K (open symbols). Dot lines show the theoretical |S| *vs.* n dependence

considering a SPB model and the effective mass (m*) that matches the Seebeck coefficient of bare Bi_2Te_3 at 300 K (black line) and 460 K (purple line).

We associate the large S values measured from Bi_2Te_3-$Cu_{2-x}Te$ composites to an energy-dependent differential scattering of charge carriers at energy barriers, i.e. to an energy filtering effect. Figure S5 shows the band alignment of the two materials as obtained from density functional theory (DFT) calculations. Owing to the large difference in electron affinity between $Cu_{2-x}Te$ and Bi_2Te_3, when nanodomains of the two materials are combined, the heavily doped $Cu_{2-x}Te$ injects electrons to Bi_2Te_3, modifying the electron energy band structure of both materials at their interphase (Figure 7a). Within the nanocomposites, the Bi_2Te_3 region nearby the heterojunction becomes flooded with electrons and its energy bands suffer an important downward bending. Taking into account the small diameter of the Bi_2Te_3 nanowires, all the nanowire region in contact with a $Cu_{2-x}Te$ domain may become flooded with electrons. These electrons need to overcome an energy barrier to exit the created potential well and freely move through the nanowire which in part explains the stronger temperature dependence of the transport properties of the composites (Figure 7b,c). Besides, the presence of these potential wells can generate a differential charge carrier mobility as a function of the carrier energy. High energy electrons should be able to freely move through Bi_2Te_3 domains within Bi_2Te_3-$Cu_{2-x}Te$ composites without a major influence of the potential wells. On the other hand, low energy electrons within Bi_2Te_3 might become trapped or scattered in these potential wells. We hypothesize this energy filtering mechanism to be responsible of the higher Seebeck coefficients displayed by Bi_2Te_3-$Cu_{2-x}Te$ composites.

The enhancement of the Seebeck coefficient associated with the energy filtering effect competes with the decrease of the Seebeck coefficient associated with the larger charge carrier concentrations. These two competing effects result in a non-monotonous dependence of the Seebeck coefficient with the amount of $Cu_{2-x}Te$ introduced. The highest Seebeck coefficients

were reached with the Bi_2Te_3-$Cu_{2-x}Te$ nanocomposite with Bi:Cu=21, which provided a S = -170 μV/K at 458 K.

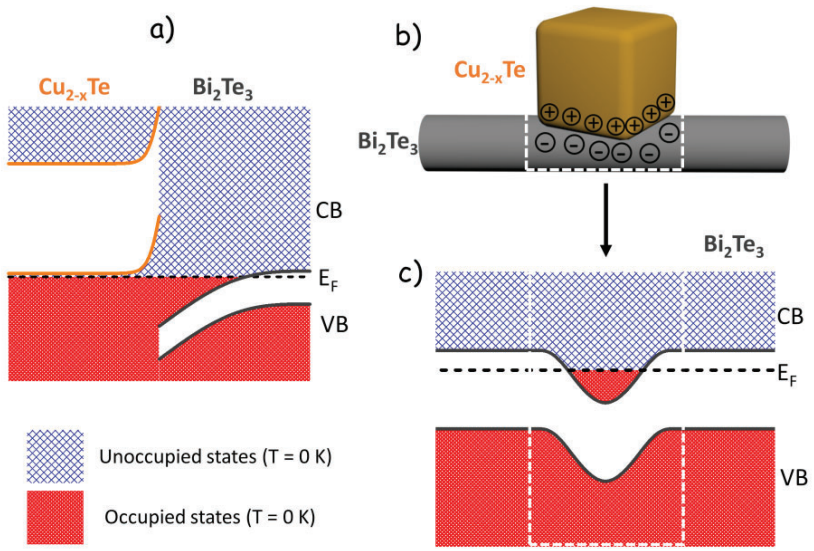

Figure 7. (a) Electron energy band diagram at a heterojunction between $Cu_{2-x}Te$ and Bi_2Te_3. (c) Charge distribution at the heterojunction between a Bi_2Te_3 nanowire and a $Cu_{2-x}Te$ cubic particle. (d) Energy band diagram of a Bi_2Te_3 nanowire in contact with a $Cu_{2-x}Te$ nanoparticle.

The thermal conductivities of all the nanomaterials were very low when compared with that of highly crystalline Bi_2Te_3. Surprisingly, the total thermal conductivities of Bi_2Te_3-$Cu_{2-x}Te$ nanocomposites were not significantly lower than those of the Bi_2Te_3 nanomaterial (Figure 5e). A slight decrease of the lattice thermal conductivity obtained in some samples and associated with an enhanced phonon scattering in the composite was compensated by an increase of the electronic contribution.

Figure 5f displays the TE figure of merit obtained from Bi_2Te_3-$Cu_{2-x}Te$ nanocomposites and the bare Bi_2Te_3 nanomaterial. For Bi_2Te_3, a maximum ZT = 0.38 was achieved at 560 K, which is a notable value for pure Bi_2Te_3.[45] As for Bi_2Te_3-$Cu_{2-x}Te$ nanocomposites, the largest ZT value was obtained from the Bi:Cu=21 sample, reaching a ZT = 0.95 at 576 K. The extraordinary improvement of figure of merit obtained with Bi_2Te_3-$Cu_{2-x}Te$ nanocomposites

was associated to two factors: (1) An effective electron spillover from $Cu_{2-x}Te$ nanoinclusions to the Bi_2Te_3 matrix that promoted electrical conductivity; and (2) the energy filtering of charge carriers at energy wells introduced within the Bi_2Te_3 matrix by the nearby presence of $Cu_{2-x}Te$ domains, and which significantly enhanced the Seebeck coefficient.

4. Conclusion

In summary, we detailed a simple bottom-up procedure to produce Bi_2Te_3-$Cu_{2-x}Te$ nanocomposites with an adjusted composition based on combining proper ratios of solution-processed Bi_2Te_3 and $Cu_{2-x}Te$ nanoparticle building blocks. With the introduction of $Cu_{2-x}Te$, the electrical conductivity of Bi_2Te_3 was greatly improved at temperatures above 400 K by charge carrier spillover from the lower work function $Cu_{2-x}Te$ domains to the Bi_2Te_3 matrix. This electron spillover from the $Cu_{2-x}Te$ valence band to the Bi_2Te_3 conduction band resulted in regions of accumulated electrons within the Bi_2Te_3 domains. In these composites, the Seebeck coefficient was significantly increased by the filtering of low energy carriers at the potential wells created in Bi_2Te_3 domains next to a Bi_2Te_3/$Cu_{2-x}Te$ heterojunction. The enhanced Seebeck coefficients and improved electrical conductivities resulted in a threefold increase in power factor. Nanocomposites did not provide lower thermal conductivities than bare Bi_2Te_3 since the thermal conductivity of all the tested nanomaterials was already very low. Overall, a significant improvement of the figure of merit was observed, from 0.35 obtained for nanocrystalline Bi_2Te_3 to 0.95 for a Bi_2Te_3-$Cu_{2-x}Te$ containing around 4 wt% of $Cu_{1.5}Te$.

Declaration of Competing Interest

The authors declare that they have no known competing financial interests or personal relationships that could have appeared to influence the work reported in this paper.

Acknowledgements

This work was supported by the European Regional Development Funds and by the Generalitat de Catalunya through the project 2017SGR1246. Y.Z, C.X, M.L, K.X and X.H thank the China Scholarship Council for the scholarship support. MI acknowledges financial support from IST Austria. YL acknowledges funding from the European Union's Horizon 2020 research and innovation program under the Marie Sklodowska-Curie grant agreement No. 754411. ICN2 acknowledges funding from Generalitat de Catalunya 2017 SGR 327 and the Spanish MINECO project ENE2017-85087-C3. ICN2 is supported by the Severo Ochoa program from the Spanish MINECO (grant no. SEV-2017-0706) and is funded by the CERCA Program/Generalitat de Catalunya. Part of the present work has been performed in the framework of Universitat Autònoma de Barcelona Materials Science PhD program.

Reference

[1] C. Wood, Materials for thermoelectric energy conversion, Rep. Prog. Phys. 51 (1988) 459.

[2] G.J. Snyder, E.S. Toberer, Complex thermoelectric materials, Nat. Mater. 7 (2008), 105-114.

[3] J.R. Sootsman, D.Y. Chung, M.G. Kanatzidis, New and old concepts in thermoelectric materials, Angew. Chem. Int. Ed. 48 (2009) 8616-8639.

[4] S. Ortega, M. Ibáñez, Y. Liu, Y. Zhang, M.V. Kovalenko, D. Cadavid, A. Cabot, Bottom-up engineering of thermoelectric nanomaterials and devices from solution-processed nanoparticle building blocks, Chem. Soc. Rev. 46 (2017) 3510-3528.

[5] X.L. Shi, X. Tao, J. Zou, Z.G. Chen, High-Performance Thermoelectric SnSe: Aqueous Synthesis, Innovations, and Challenges, Adv. Sci. 7 (2020) 1902923.

[6] D. Cadavid, S. Ortega, S. Illera, Y. Liu, M. Ibáñez, A. Shavel, Y. Zhang, M. Li, A.M. López, G.n. Noriega, Influence of the Ligand Stripping on the Transport Properties of Nanoparticle-Based PbSe Nanomaterials, ACS Appl. Energy Mater. (2020).

[7] S. Roychowdhury, R.K. Biswas, M. Dutta, S.K. Pati, K. Biswas, Phonon Localization and

Entropy-Driven Point Defects Lead to Ultralow Thermal Conductivity and Enhanced Thermoelectric Performance in $(SnTe)_{1-2x}(SnSe)_x(SnS)_x$, ACS Energy Lett. 4 (2019) 1658-1662.

[8] M. Ibáñez, R. Hasler, A. Genç, Y. Liu, B. Kuster, M. Schuster, O. Dobrozhan, D. Cadavid, J. Arbiol, A. Cabot, Ligand-Mediated Band Engineering in Bottom-Up Assembled SnTe Nanocomposites for Thermoelectric Energy Conversion, J. Am. Chem. Soc. 141 (2019) 8025-8029.

[9] M. Ibáñez, A. Genç, R. Hasler, Y. Liu, O. Dobrozhan, O. Nazarenko, M.a.d.l. Mata, J. Arbiol, A. Cabot, M.V. Kovalenko, Tuning transport properties in thermoelectric nanocomposites through inorganic ligands and heterostructured building blocks, ACS nano 13 (2019) 6572-6580.

[10] S. Chandra, K. Biswas, Realization of high thermoelectric figure of merit in solution synthesized 2D SnSe nanoplates via Ge alloying, J. Am. Chem. Soc. 141 (2019) 6141-6145.

[11] Y. Zhang, Y. Liu, K.H. Lim, C. Xing, M. Li, T. Zhang, P. Tang, J. Arbiol, J. Llorca, K.M. Ng, Tin Diselenide Molecular Precursor for Solution-Processable Thermoelectric Materials, Angew. Chem. 130 (2018) 17309-17314.

[12] Y. Liu, Y. Zhang, S. Ortega, M. Ibáñez, K.H. Lim, A. Grau-Carbonell, S. Martí-Sánchez, K.M. Ng, J. Arbiol, M.V. Kovalenko, Crystallographically Textured Nanomaterials Produced from the Liquid Phase Sintering of $Bi_xSb_{2-x}Te3$ Nanocrystal Building Blocks, Nano Lett. 18 (2018) 2557-2563.

[13] Y. Liu, Y. Zhang, K.H. Lim, M. Ibáñez, S. Ortega, M. Li, J. David, S. Martí-Sánchez, K.M. Ng, J. Arbiol, High Thermoelectric Performance in Crystallographically Textured n-Type Bi2Te3–x Se x Produced from Asymmetric Colloidal Nanocrystals, ACS nano 12 (2018) 7174-7184.

[14] M. Ibáñez, R. Hasler, Y. Liu, O. Dobrozhan, O. Nazarenko, D. Cadavid, A. Cabot, M.V. Kovalenko, Tuning p-Type Transport in Bottom-Up Engineered Nanocrystalline Pb Chalcogenides Using Alkali Metal Chalcogenides as Capping Ligands, Chem. Mater. 29 (2017)

7093-7097.

[15] Y. Liu, D. Cadavid, M. Ibáñez, S. Ortega, S. Martí-Sánchez, O. Dobrozhan, M.V. Kovalenko, J. Arbiol, A. Cabot, Thermoelectric properties of semiconductor-metal composites produced by particle blending, Apl Mater. 4 (2016) 104813.

[16] M. Ibáñez, R.J. Korkosz, Z. Luo, P. Riba, D. Cadavid, S. Ortega, A. Cabot, M.G. Kanatzidis, Electron doping in bottom-up engineered thermoelectric nanomaterials through HCl-mediated ligand displacement, J. Am. Chem. Soc. 137 (2015) 4046-4049.

[17] Y. Min, J.W. Roh, H. Yang, M. Park, S.I. Kim, S. Hwang, S.M. Lee, K.H. Lee, U. Jeong, Surfactant‐Free Scalable Synthesis of Bi_2Te_3 and Bi_2Se_3 Nanoflakes and Enhanced Thermoelectric Properties of Their Nanocomposites, Adv. Mater. 25 (2013) 1424-1424.

[18] B. Yu, M. Zebarjadi, H. Wang, K. Lukas, H. Wang, D. Wang, C. Opeil, M. Dresselhaus, G. Chen, Z. Ren, Enhancement of thermoelectric properties by modulation-doping in silicon germanium alloy nanocomposites, Nano Lett. 12 (2012) 2077-2082.

[19] J.P. Heremans, C.M. Thrush, D.T. Morelli, Thermopower enhancement in PbTe with Pb precipitates, J. Appl. Phys 98 (2005) 063703.

[20] D. Bao, J. Chen, Y. Yu, W. Liu, L. Huang, G. Han, J. Tang, D. Zhou, L. Yang, Z.-G. Chen, Texture-dependent thermoelectric properties of nano-structured Bi_2Te_3, Chem. Eng. J. 388 (2020) 124295.

[21] Y. Liu, M. Zhou, J. He, Towards higher thermoelectric performance of Bi_2Te_3 via defect engineering, Scr. Mater. 111 (2016) 39-43.

[22] M. Hong, Z.G. Chen, L. Yang, J. Zou, $Bi_xSb_{2-x}Te_3$ nanoplates with enhanced thermoelectric performance due to sufficiently decoupled electronic transport properties and strong wide-frequency phonon scatterings, Nano Energy 20 (2016) 144-155.

[23] M. Hong, T.C. Chasapis, Z.-G. Chen, L. Yang, M.G. Kanatzidis, G.J. Snyder, J. Zou, n-Type $Bi_2Te_{3-x}Se_x$ Nanoplates with Enhanced Thermoelectric Efficiency Driven by Wide-

Frequency Phonon Scatterings and Synergistic Carrier Scatterings, ACS nano 10 (2016) 4719-4727.

[24] L. Hu, T. Zhu, X. Liu, X. Zhao, Point defect engineering of high-performance Bismuth-Telluride-based thermoelectric materials, Adv. Funct. Mater. 24 (2014) 5211-5218.

[25] A. Soni, Y. Shen, M. Yin, Y. Zhao, L. Yu, X. Hu, Z. Dong, K.A. Khor, M.S. Dresselhaus, Q. Xiong, Interface driven energy filtering of thermoelectric power in spark plasma sintered $Bi2Te_{2.7}Se_{0.3}$ nanoplatelet composites, Nano Lett. 12 (2012) 4305-4310.

[26] X. Yan, B. Poudel, Y. Ma, W. Liu, G. Joshi, H. Wang, Y. Lan, D. Wang, G. Chen, Z. Ren, Experimental studies on anisotropic thermoelectric properties and structures of n-type $Bi_2Te_{2.7}Se_{0.3}$, Nano Lett. 10 (2010) 3373-3378.

[27] L.-D. Zhao, B.-P. Zhang, W.-S. Liu, J.-F. Li, Effect of mixed grain sizes on thermoelectric performance of Bi_2Te_3 compound, J. Appl. Phys. 105 (2009) 023704.

[28] L. Zhao, B.-P. Zhang, W. Liu, H. Zhang, J.-F. Li, Effects of annealing on electrical properties of n-type Bi_2Te_3 fabricated by mechanical alloying and spark plasma sintering, J. Alloys Compd. 467 (2009) 91-97.

[29] L.-D. Zhao, B.-P. Zhang, J.-F. Li, M. Zhou, W.-S. Liu, J. Liu, Thermoelectric and mechanical properties of nano-SiC-dispersed Bi_2Te_3 fabricated by mechanical alloying and spark plasma sintering, , J. Alloys Compd. 455 (2008) 259-264.

[30] B. Poudel, Q. Hao, Y. Ma, Y. Lan, A. Minnich, B. Yu, X. Yan, D. Wang, A. Muto, D. Vashaee, High-thermoelectric performance of nanostructured bismuth antimony telluride bulk alloys, Science 320 (2008) 634-638.

[31] W. Zhu, W. Hu, P. Wei, X. Nie, W. Zhao, Preparation and Enhanced Thermoelectric Properties of $Cu/Bi_{0.5}Sb_{1.5}Te_3$ Composite Materials, J. Electron. Mater. (2020) 1-6.

[32] M. Sinduja, S. Amirthapandian, A. Masarrat, R. Krishnan, S. Srivastava, A. Kandasami, Investigations on morphology and thermoelectric transport properties of Cu^+ ion implanted bismuth telluride thin film, Thin Solid Films 697 (2020) 137834.

[33] H.-L. Zhuang, Y. Pan, F.-H. Sun, J. Dong, J. Pei, B. Cai, H. Hu, H. Tang, J.-F. Li, Thermoelectric Cu-doped (Bi, Sb)$_2$Te$_3$: performance enhancement and stability against high electric current pulse, Nano Energy 60 (2019) 857-865.

[34] J.M. Song, J.U. Rahman, J.Y. Cho, S. Lee, W.S. Seo, S. Kim, S.-i. Kim, K.H. Lee, D. Roh, W.H. Shin, Chemically synthesized Cu_2Te incorporated Bi-Sb-Te p-type thermoelectric materials for low temperature energy harvesting, Scr. Mater. 165 (2019) 78-83.

[35] H.-J. Wu, W.-T. Yen, High thermoelectric performance in Cu-doped Bi_2Te_3 with carrier-type transition, Acta Mater. 157 (2018) 33-41.

[36] K.H. Seo, B.G. Kim, C.-H. Lim, S.-H. Kim, K.-M. Lee, J.-Y. Kim, S.-M. Choi, Doping amount dependence of phase formation and microstructure evolution in heavily Cu-doped Bi_2Te_3 films for thermoelectric applications, CrystEngComm 19 (2017) 2750-2757.

[37] Q. Lognoné, F. Gascoin, Reactivity, stability and thermoelectric properties of n- Bi_2Te_3 doped with different copper amounts, , J. Alloys Compd. 610 (2014) 1-5.

[38] W.S. Liu, Q. Zhang, Y. Lan, S. Chen, X. Yan, Q. Zhang, H. Wang, D. Wang, G. Chen, Z. Ren, Thermoelectric property studies on Cu-doped n-type $CuxBi_2Te_{2.7}Se_{0.3}$ nanocomposites, Adv. Energy Mater. 1 (2011) 577-587.

[39] J. Bludska, I. Jakubec, Č. Drašar, P. Lošťák, J. Horak, Structural defects in Cu-doped Bi_2Te_3 single crystals, Philoss Mag. 87 (2007) 325-335.

[40] M. Huang, A. Maljusch, F. Calle-Vallejo, J.B. Henry, M.T. Koper, W. Schuhmann, A.S. Bandarenka, Electrochemical formation and surface characterisation of $Cu_{2-x}Te$ thin films with adjustable content of Cu, RSC Advances 3 (2013) 21648-21654.

[41] K. Zhao, K. Liu, Z. Yue, Y. Wang, Q. Song, J. Li, M. Guan, Q. Xu, P. Qiu, H. Zhu, Are Cu_2Te-Based Compounds Excellent Thermoelectric Materials?, Adv. Mater. 31 (2019) 1903480.

[42] Y. Qiu, Y. Liu, J. Ye, J. Li, L. Lian, Synergistic optimization of carrier transport and thermal conductivity in Sn-doped Cu_2Te, J. Mater. Chem. A 6 (2018) 18928-18937.

[43] M.M. Mallick, S. Vitta, Realizing high figure-of-merit in Cu_2Te using a combination of doping, hierarchical structure, and simple processing, J. Appl. Phys. 122 (2017) 024903.

[44] S. Ballikaya, H. Chi, J.R. Salvador, C. Uher, Thermoelectric properties of Ag-doped Cu_2Se and Cu 2 Te, J. Mater. Chem. A 1 (2013) 12478-12484.

[45] Y. Zhang, Y. Liu, M. Calcabrini, C. Xing, X. Han, J. Arbiol, D. Cadavid, M. Ibáñez, A. Cabot, Bismuth telluride–copper telluride nanocomposites from heterostructured building blocks, J. Mater. Chem. C 8 (2020) 14092-14099.

[46] G. Zhang, B. Kirk, L.A. Jauregui, H. Yang, X. Xu, Y.P. Chen, Y. Wu, Rational synthesis of ultrathin n-type Bi_2Te_3 nanowires with enhanced thermoelectric properties, Nano Lett. 12 (2012) 56-60.

[47] T. Willhammar, K. Sentosun, S. Mourdikoudis, B. Goris, M. Kurttepeli, M. Bercx, D. Lamoen, B. Partoens, I. Pastoriza-Santos, J. Pérez-Juste, Structure and vacancy distribution in copper telluride nanoparticles influence plasmonic activity in the near-infrared, Nat. commun. 8 (2017) 1-7.

[48] W. Li, R. Zamani, P. Rivera Gil, B. Pelaz, M. Ibáñez, D. Cadavid, A. Shavel, R.A. Alvarez-Puebla, W.J. Parak, J. Arbiol, CuTe nanocrystals: shape and size control, plasmonic properties, and use as SERS probes and photothermal agents, J. Am. Chem. Soc. 135 (2013) 7098-7101.